NJC

ROYAL SOCIETY OF CHEMISTRY

PAPER

Cite this: *New J. Chem.*, 2023, **47**, 2874

# Crystallographic characterization and application of copper doped hydroxyapatite as a biomaterial

Supanna Malek Tuntun,[ab] Md. Sahadat Hossain, [a] Md. Najem Uddin, [c] Md. Aftab Ali Shaikh,[acd] Newaz Mohammed Bahadur[b] and Samina Ahmed *[ac]

Received 18th August 2022,
Accepted 2nd January 2023

DOI: 10.1039/d2nj04130h

rsc.li/njc

Hydroxyapatite (HAp) is a prominent biomaterial used as an effective implant material in bone tissue engineering. This research work reports the synthesis of copper (Cu) doped hydroxyapatite (HAp) with an enhancement of properties for advanced applications in biomedical sectors. By varying the percentages of Cu (0, 5, and 10%), the desired doped samples were prepared. By employing X-ray diffraction (XRD) and Fourier transform infrared (FT-IR) spectroscopy, the characterization of the synthesized materials was performed. Using the XRD data, different crystallographic parameters like microstrain, crystallinity index, lattice parameters, HAp percentage, dislocation density, specific area, degree of crystallinity, and preferential growth were evaluated along with crystallite size with the aid of different model equations. The biocompatibility of the prepared doped HAp samples was explored through haemolysis tests, cytotoxicity analysis, and antimicrobial activity study (using both Gram-positive and Gram-negative bacteria). The observed results confirm 5% Cu-doped hydroxyapatite as a good choice for use in biomedical fields.

## Introduction

Having vast application potential, hydroxyapatite (HAp) is categorically ranked as one of the most well-known biomaterials. It has been extensively used in the biomedical field due to its chemical similarity with human hard tissue.[1] HAp possesses exceptional osteoconductivity, biocompatibility, chemical stability, non-toxicity and non-immunogenic properties.[2–7] These advantageous and versatile characteristics enable HAp to be used in various applications like bone replacement, defected bone fillers in clinical orthopedics, dental implants, knee or hip replacement, tooth paste additives, control drug release systems *etc.*[8–10] Retaining its hexagonal structure, HAp belongs to the $P6_3/m$ space group while its unit cell contains ten Ca ions situated at two different positions: (i) the $Ca_1$ site, which holds four cations surrounded by nine oxide ions ($O^{2-}$); and (ii) the $Ca_2$ site containing six cations enclosed with seven oxide ions. However, in conjunction with the Ca ions, six phosphate and two hydroxyl groups also exist in the HAp unit cell. This structural arrangement of HAp allows both anionic and cationic doping to enhance its properties.

Nevertheless, apart from HAp, some other notable biomaterials such as hydrogels,[11] collagen, chitosan, starch, alginates,[12] different polymer materials like polyphosphazenes,[13] polyorganophosphazenes,[14] polyphosphoesters (PPEs),[15] polyurethane (PU),[16] polyanhydrides,[17] and polycaprolactone,[18] bioactive glasses[19] *etc.* have attracted the attention of researchers. However, some selective benchmarks have graded HAp as the best choice. Hence, we have focused on HAp but given particular attention to exploring its doped form. Fusion of metal ions like $Mg^{2+}$, $Zn^{2+}$, $Cd^{2+}$,[20] $Mn^{2+}$, $Ca^{2+}$, $Ag^{+}$, $Pb^{2+}$, $Co^{2+}$ *etc.* or heavy metals into the structure of HAp increases the rate of cation exchange[21] and modifies other properties such as solubility, chemical stability,[22] degree of crystallinity,[23] antimicrobial activity[24] and mechanical properties. HAp with metal ion dopants shows significant changes in its structural as well as physicochemical and biological characteristics; *e.g.*, HAp in its doped form triggers speedy bone formation, enables strong bond construction between living cells and grafts and causes the function of osteoblasts to flourish inside the human body.[25–27] Owing to its pro-angiogenic potential as well as ability to stimulate endothelial cell proliferation both *in vitro* and *in vivo*, recently, copper (Cu) ion has been gaining interest as a doping candidate.[28] Moreover, its antibacterial efficiency is also taken into account in the case of doping. Indeed, in comparison with the pristine HAp, a higher antimicrobial response of Cu-doped HAp was noticed in a previous study.[29] Although the presence of Cu in small amounts is essential for numerous activities in living entities as it promotes metabolism and bone growth, it can potentially become toxic when the limiting boundary is crossed.[30] Interestingly, a few previous research papers

---

[a] *Institute of Glass & Ceramic Research and Testing, Bangladesh Council of Sientific and Industrial Research (BCSIR), Dhaka 1205, Bangladesh. E-mail: shanta_samina@yahoo.com*
[b] *Department of Applied Chemistry and Chemical Engineering, Noakhali Science and Technology University, Noakhali, Bangladesh*
[c] *BCSIR Laboratories Dhaka, Bangladesh Council of Scientific and Industrial Research (BCSIR), Dhaka 1205, Bangladesh*
[d] *Department of Chemistry, University of Dhaka, Dhaka-1000, Bangladesh*

stated that Cu substitution in HAp is not a straightforward job. The ionic radii of $Cu^+$ and $Cu^{2+}$ and the doped amount of Cu are two factors that guide the substitution occurring at Ca sites or in the interstitial positions along the hexagonal channel,[30].[31]

Gomes *et al.*[32] in their research paper described in detail the phase composition and copper insertion position coupled with its electronic state. They also investigated the temperature-dependent Cu assimilation mechanism. The observations of this study revealed that at an applied temperature of $<1100$ °C, a small number of Cu ions were incorporated while an elevated temperature $>1100$ °C facilitated enriched doping of Cu. However, a higher temperature causes Cu ions to depart from the HAp lattice thus forming CuO, perhaps by mingling with $O^{2-}$ anions of the hydroxyl channel. Regarding all these facts, in this research work, we have attempted to synthesize Cu-doped HAp using various percentages of doping ion solution at a calcination temperature $<1100$ °C (900 °C). Since our intention was to achieve Cu exchange solely for Ca ions and not for hydroxyl groups, we categorically chose a temperature $<1100$ °C.[33] The goal of this initiative was to introduce enhanced biological functions in the targeted doped HAp that could make it beneficial as a biomaterial.

# Materials and methods

### Materials

Ortho phosphoric acid ($H_3PO_4$), calcium hydroxide ($Ca(OH)_2$), ammonium hydroxide ($NH_4OH$), nitric acid ($HNO_3$) and cupric oxide (CuO) were purchased from E-Merck Germany and used as received. All the chemicals used in this work were of analytical grade. A double distillation process facilitated the preparation of deionized (DI) water.

### Synthesis of pure and Cu doped Hydroxyapatite (HAp)

Keeping the Ca/P ratio at 1.67, pure and Cu-doped HAp were prepared by a conventional wet chemical precipitation method while the Ca and P sources were $Ca(OH)_2$ and $H_3PO_4$, respectively.[34] An equal volume of 1.67 M $Ca(OH)_2$ and 1.0 M $H_3PO_4$ solution was prepared for the synthesis of HAp using DI water. $H_3PO_4$ was added to the $Ca(OH)_2$ solution at a rate of 3.0 mL $m^{-1}$, while the reaction conditions were: (i) solution pH: 10–11 (maintained by adding $NH_4OH$ solution); and (ii) reaction temperature: ambient. Continuous stirring was applied until the completion of the reaction. Subsequently, a precipitate formed that was filtered out and oven-dried at 105 °C for 24 h. The whole dried portion was powdered and subjected to calcination at 900 °C for 1/2 h (rate of calcination temperature increase was 3.5 °C $m^{-1}$). The same methodology was performed for the Cu doped HAp. In this case, using $HNO_3$ acid, a 1.67 M CuO solution was prepared with $x$% ($x$ = 5 and 10%) Cu and added to the $H_3PO_4$ solution. Cu-doped HAp samples were labeled as 5-Cu HAp and 10-Cu HAp. The chemical reactions that occurred during the synthesis process are presented in eqn (1)–(3).

$$10Ca(OH)_2 + 6H_3PO_4 \rightarrow Ca_{10}(PO_4)_6(OH)_2 \tag{1}$$

$$CuO + 2HNO_3 \rightarrow \text{Cu-solution} \tag{2}$$

$$x\,Ca(OH)_2 + y\,\text{Cu-solution} + 6H_3PO_4 \rightarrow Ca_{x-y}Cu_y(PO_4)_6(OH)_2 \tag{3}$$

# Characterization

### X-ray diffraction (XRD) study

A Rigaku SE XRD (X-ray diffractometer) machine with a Copper radiation source was employed to record the X-ray diffractograms of the prepared samples under 40 mA and 50 kV operating conditions. Cu Kα radiation ($\lambda$ = 1.5406 A) was used to record the XRD patterns of the powdered samples in the scanning range of $2\theta = 15$–$70°$ in steps of 0.01. From the collected data, various crystallographic parameters such as lattice parameters, cell volume, crystallinity index, dislocation density, crystallite size, degree of crystallinity, microstrain, and HAp percentage were computed using eqn (4)–(10).[35]

$$\text{Lattice parameter equation,}\ \left(\frac{1}{d_{hkl}}\right)^2 = \frac{4}{3}\left(\frac{h^2+hk+k^2}{a^2}\right) + \frac{l^2}{c^2} \tag{4}$$

$$\text{Cell volume,}\ V = \frac{\sqrt{3}}{2}a^2c \tag{5}$$

$$\text{Crystallite size,}\ D_c = \frac{K\lambda}{\beta\cos\theta} \tag{6}$$

$$\text{Degree of crystallinity,}\ X_c = \left(\frac{K_a}{\beta}\right)^3 = \left(\frac{0.24}{\beta}\right)^3 \tag{7}$$

$$\text{Dislocation density,}\ \delta = \frac{1}{(D_c)^2} \tag{8}$$

$$\text{Crystallinity index,}\ CI_{XRD} = \sum\frac{H_{(202)}+H_{(300)}+H_{(112)}}{H_{(211)}} \tag{9}$$

$$\text{Crystallinity index}\ CI_{112/300} = 1 - \frac{V_{112/300}}{I_{300}} \tag{10}$$

where $\beta$ = FWHM (full width at half maximum) in radian, $\delta$ = dislocation density, $K$ = shape factor (arbitrary constant)/Scherrer's constant = 0.94; $D_c$ = crystallite size, $\theta$ = diffraction angle (in degree), $H_{(hkl)}$ = peak height of the respective plane, $X_c$ = degree of crystallinity, $K_a$ = constant = 0.24 for HAp, and CIXRD = crystallinity index. In eqn (4), ($h$,$k$,$l$) represents the plane of the unit cell and $a$, $b$, $c$ are the crystallographic lattice parameters.

### Fourier-transform infrared (FT-IR) spectral analysis

To define the functional groups of HAp and Cu-doped HAp, a FT-IR spectrophotometer (IR-Prestige 21, Shimadzu, Japan) equipped with an attenuated total reflectance (ATR) facility was used. The spectra were recorded with a spectral resolution of 4 $cm^{-1}$ in the range of 4000–400 $cm^{-1}$ using 30 scans.

### Microstructural and elemental analysis

A high resolution Field Emission Scanning Electron Microscopy (FESEM) (Model JEOL JSM-7610F) instrument equipped with an energy dispersive spectroscopy (EDS) facility was used for microstructural and elemental analysis of Cu-doped Hap samples.

### Cytotoxicity evaluation

Cytotoxicity is an important parameter used to check the toxicity levels of biomaterials towards bodily cells after application in the human body. The Trypan Blue Exclusion method was employed, which simplifies a difference between viable and non-viable cells,[36,37] for the measurement of cytotoxicity of the synthesized samples. A vero cell line (CLS 605372, Germany) was collected from African green monkey kidney cells and used to perform the cytotoxicity experiments, as detailed in a previous investigation.[36,37] Eqn (11) was employed to calculate the percentage cytotoxicity.[38]

$$\text{Percentage of viable cells} = \frac{\text{Number of viable cells}}{\text{Total number of cells}} \times 100 \quad (11)$$

### Haemolytic assay

To evaluate the biomedical application potential of the pure and Cu doped HAp, a haemolysis test was performed. Haemolysis is the process of rapturing or releasing hemoglobin from human red blood cells (RBCs). However, to conduct this experiment, the anti-coagulant heparin was added to the freshly collected human blood sample followed by one h incubation at 37 °C.[39] Distilled water was chosen as the positive control while a physiological saline extract solution was used as the negative control. For each set of experiments, a known amount of the sample (500 $\mu$g mL$^{-1}$ with 0.4 mL of human blood) was incubated for one h at 37 °C followed by 5 m in the centrifuge at 3000 rpm. The absorbance of the supernatant was logged at 545 nm and the following expression was employed to calculate the haemolysis percentage of blood ($H_b$),

$$H_b = \frac{A_s - A_{nc}}{A_{pc} - A_{nc}} \times 100 \quad (12)$$

where $A_s$ denotes the average absorbance of the samples, and $A_{pc}$ and $A_{nc}$ are the absorbance of the positive and negative controls, respectively.

### Assessment of antimicrobial activity

The antimicrobial activity of the prepared samples was examined by employing the media poisoning technique.[39] Two different types of bacteria, *Escherichia coli* (*E. coli*, ATCC-11303, Gram-negative bacteria) and *Staphylococcus aureus* (*S. aureus*, ATCC-9144, Gram-positive bacteria), were chosen to study the antimicrobial activity of the pure and Cu doped HAp samples. To assess the antimicrobial activity, each sample (1 mg mL$^{-1}$) was mixed with 15 mL of nutrient agar medium followed by sterilization for a certain period at a pressure of 15 lbs. The sterilized sample was then placed into an aseptic Petri dish and, with the help of a glass spreader, 400 $\mu$L of organisms from the fresh cultured media of the chosen bacteria that was diluted 15 times was placed on the Petri dish and left overnight. Sterilized conditions were applied at this step while using the glass spreader. The dish was then incubated at room temperature and left for 24 h in the turn down position. A number of colonies was formed with the fresh culture media after the incubation time was over. The bactericidal rate ($B_r$) was obtained by counting the number of colonies with the help of eqn (14), where $C_c$ and $C_s$ represent colonies formed at the control and sample, respectively.

$$B_r = \frac{C_c - C_s}{C_c} \times 100\% \quad (13)$$

## Results and discussion

### Characterization of HAp, 5-Cu HAp and 10-Cu HAp

**X-ray diffraction analysis.** The XRD patterns of the prepared HAp, 5-Cu HAp and 10-Cu HAp are shown in Fig. 1. Coupled with the XRD patterns of HAp, a few characteristic reflections for $\beta$-tricalcium phosphate ($\beta$-TCP) also appeared in all three diffractograms, which revealed that the formation of pure and doped HAp occurred in a biphasic form. The $2\theta$ positions for the HAp phase were noticed at 25.93° (002), 31.83° (211), 32.24° (112), 32.96° (300), 34.12° (202), 39.88° (130), 46.75° (222) and 49.53° (213), which were well-aligned with the standard ICDD database (card no: 01-074-0565) for HAp and a hexagonal crystal structure was confirmed.

However, substitution of various cations into the HAp structure depends on the size of the ionic radius and thus substitution can change the crystallographic parameters of HAp. Usually, cations possessing a small ionic radius as compared to $Ca^{2+}$ prefer $Ca_1$ sites for incorporation and this results in a contraction along the *a*- and *c*-axes. On the other hand, cations having a larger ionic radius choose $Ca_2$ sites for substitution. Consequently, since the ionic radius of Cu ions ($Cu^+$ = 0.96 Å and $Cu^{2+}$ = 0.72 Å) is smaller than that of $Ca^{2+}$ (0.99 Å), substitution of $Ca^{2+}$ in HAp by Cu ions favored $Ca_1$ sites, which was confirmed by the calculated lattice parameter values, as charted in Table 1. Considering the (002) and (300) planes, the lattice parameters of HAp, 5-Cu HAp and 10-Cu HAp were calculated using eqn (4) and (5). Clearly, the lattice parameter shrinkage follows the order: 10-Cu HAp < 5-Cu Hap < HAp as expected and this decreasing nature in lattice parameter values was also noticed in a previous investigation.[29]

Other associated crystallographic parameters of HAp were calculated using eqn (6)–(11) and the corresponding values are summarized in Table 1. Since, for both pure and Cu-doped HAp samples the reflection of the (211) plane was logged as the most distinct, the mean crystallite size of all the samples was worked out considering the line broadening of the (211) reflection. Calculated crystallite size (as shown in Table 1) tends to decrease as a function of Cu-substitution. The higher the scale of replacement, the smaller the crystallite size (Table 1).

Note, a large surface area is provided by a decreased crystallite size and this provides potential applicability of a material with significant changes in properties.[40] Using the calculated

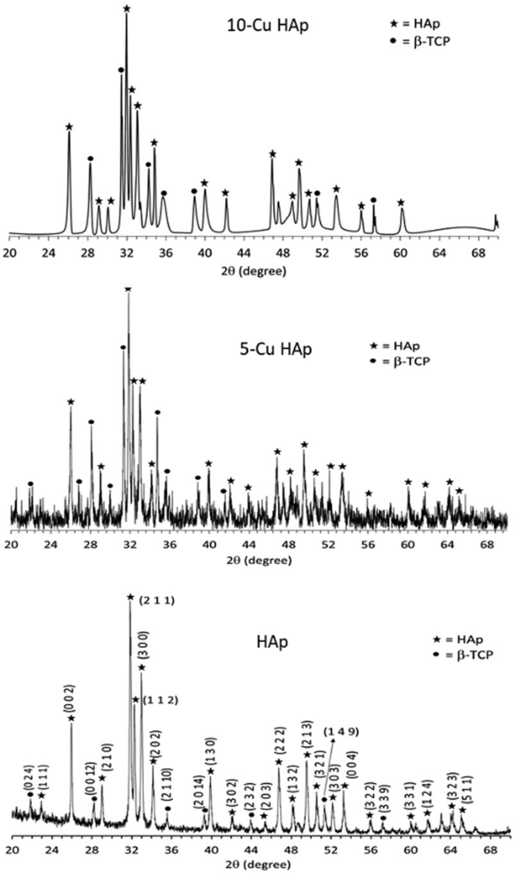

Fig. 1 X-ray diffraction patterns of pure and copper doped HAp.

crystallite size values (Table 1), the specific surface area was determined utilizing eqn (14) for the synthesized samples.

$$\text{Specific surface area, } S = \frac{6}{\rho \times D_c}\text{m}^2\text{g}^{-1} \tag{14}$$

where $D_c$ and $\rho$ represent the crystallite size and the density of the samples. By taking into account the theoretical density of HAp (3.16 g cm$^{-3}$),[41] the resultant specific surface area was estimated for each sample (Table 1). The specific surface area values gradually increased as HAp < 5-Cu HAp < 10-Cu HAp and supported the decreasing nature of crystallite size for these three samples, which in turn indicates that with the increase of the doping ion concentration, the samples become more amorphous. Consequently, the degree of crystallinity decreased but the dislocation density increased as the extent of Cu substitution in the HAp lattice increased (Table 1).

Preferential growth of hexagonal HAp and Cu doped HAp was also calculated using eqn (15).[42] The relative intensity was obtained by calculation using the (002) plane, as the ratio of the intensity of the (002) plane to the intensities of the three major peaks of the plane (211), (112) and (300). The mathematical expression is given below in eqn (16).[43]

$$\text{Preference growth, } P = \frac{\text{RI} - \text{RI}_\text{s}}{\text{RI}_\text{s}} \tag{15}$$

$$\text{Relative intensity, } \text{RI} = \frac{I_{002}}{I_{211} + I_{300} + I_{112}} \tag{16}$$

Here, in eqn (16), $\text{RI}_\text{s}$ refers to the standard relative intensity of the same plane. The calculated values of relative intensities were 0.17 (HAp), 0.19 (5 Cu HAp) and 0.25 (10 Cu HAp) and the preference growth was 0.07, 0.21 and 0.58 for the prepared samples, respectively. The high value for 10 Cu HAp indicates that the atoms are more concentrated in the respective plane due to agglomeration of the sample and this provides a lower surface energy with a stable crystal structure.

## Crystallite size calculation using various models

More accurate and precise crystallite size values can be calculated by using various model equations like the linear straight line method of Scherrer's equation, Williamson–Hall method, Monshi–Scherrer method, *etc.* But, according to our perception, these models retain some shortcomings, and hence we further proceeded to work out the crystallite size more precisely using two newly developed models as described elsewhere.[44]

## Linear straight line method of Scherrer's equation

A modified form of Scherrer's equation known as the linear straight-line method of Scherrer's equation (LSLMSE) was applied to compute the crystallite size of the HAp samples. The important criterion of this method is that it considers all peaks instead of selecting a distinctive diffraction peak.[45] By rearranging the Scherrer equation (eqn (6)), a mathematical

Table 1 Crystallographic parameters of the prepared pure and copper doped HAp

| | Name of samples | | |
|---|---|---|---|
| Crystallographic parameters | HAp | 5-Cu HAp | 10-Cu HAp |
| Crystallite size, $D_c$ (nm) | 63.06 | 61.19 | 54.01 |
| Surface area, m$^2$ g$^{-1}$ | 30.10 | 31.02 | 35.15 |
| Degree of crystallinity, $X_c$ (%) | 6.14 | 5.61 | 3.85 |
| Dislocation density, $\delta$ (line per m$^2$) | 0.25 | 0.26 | 0.34 |
| Microstrain | 0.11 | 0.12 | 0.13 |
| Percentage of HAp | 85.59 | 88.71 | 67.64 |
| Crystallinity index, $\text{CI}_\text{XRD}$ | 1.49 | 1.39 | 1.52 |
| Crystallinity index $\text{CI}_{112/300}$ | 0.75 | 0.61 | 0.79 |
| Lattice parameters | $a = b = 9.42$ Å<br>$c = 6.88$ Å<br>$V = 528.71$ Å | $a = b = 9.40$ Å<br>$c = 6.86$ Å<br>$V = 525.56$ Å | $a = b = 9.38$ Å<br>$c = 6.84$ Å<br>$V = 521.5$ Å |

expression can be written as follows:

$$\cos\theta = \frac{K\lambda}{D_{\mathrm{c}}} \times \frac{1}{\beta} = \frac{K\lambda}{D_{\mathrm{L}}} \times \frac{1}{\beta} \tag{17}$$

Here, $D_{\mathrm{L}}$ denotes crystallite size obtained from the linear straight-line method of Scherrer's equation. Fig. 2(A) shows a graphical plot where the $y$-axis ($\cos\theta$, in degree) and the $x$-axis ($\frac{1}{\beta}$, in radian) were plotted by using eqn (17) and a straight line was observed. Thus, eqn (17) can be compared with the linear straight-line equation ($y = mx + c$) and the crystallite sizes of the prepared samples were calculated by utilizing the slope $m = \frac{K\lambda}{D_{\mathrm{L}}}$ and the values obtained are listed in Table 2. This method is void because of the very large crystallite size, which is expected to be less than 100 nm.

### Williamson–Hall method

Considering the strain in the crystal, the crystallite size was calculated by employing the Williamson–Hall model. A very precise crystallite size along with crystal strain can be calculated by using the Williamson–Hall[46] method and the equation is expressed as follows:

$$\beta_{\mathrm{total}} \cos\theta = \frac{K_{\mathrm{B}}\lambda}{D_{\mathrm{W}}} + 4\varepsilon \sin\theta \tag{18}$$

A graphical scheme was plotted [Fig. 2(B)] where $\beta_{\mathrm{total}}\cos\theta$ (in radian, degree) and $4\sin\theta$ (in degree) were in the $y$-axis and $x$-axis, respectively. By comparing eqn 18 and 6, the intercept $y$ from the plot was assumed to equal $\frac{K_{\mathrm{B}}\lambda}{D_{\mathrm{W}}}$, which was then used to calculate the crystallite sizes of the synthesized HAp samples. The values are listed in the following Table 2 and are within acceptable limits in nano-scale measurement. The strains calculated using this model are 0.0008, 0.0014, and −0.0008, for HAp, 5-Cu HAp, and 10-Cu HAp, respectively.

### Monshi–Scherrer method

Considering the sharpest diffraction peak, the Monshi–Scherrer method calculates the crystallite size ($D_{\mathrm{M}}$) by rearranging and taking 'ln' in Scherrer's equation.[47] The mathematical expression is given as follows:

$$\ln\,\beta = \ln\frac{1}{\cos\theta} + \ln\frac{K\lambda}{D_{\mathrm{M}}} \tag{19}$$

A plot was made [Fig. 3(C)] using eqn (19) where $\ln\beta$ (in radian) formed the $y$-axis and $\ln\frac{1}{\cos\theta}$ (in degree) formed the $x$-axis. The crystallite size ($D_{\mathrm{M}}$) was calculated by comparing eqn (6) and (19) and the $y$-intercept was found to be equivalent to $\ln\frac{K\lambda}{D_{\mathrm{M}}}$ and the resultant values are listed in Table 2. The resultant values are in the nano range and closely matched the values obtained using the Scherrer equation, which confirms the validity of the Monshi–Scherrer method to calculate the crystallite sizes of the prepared samples.

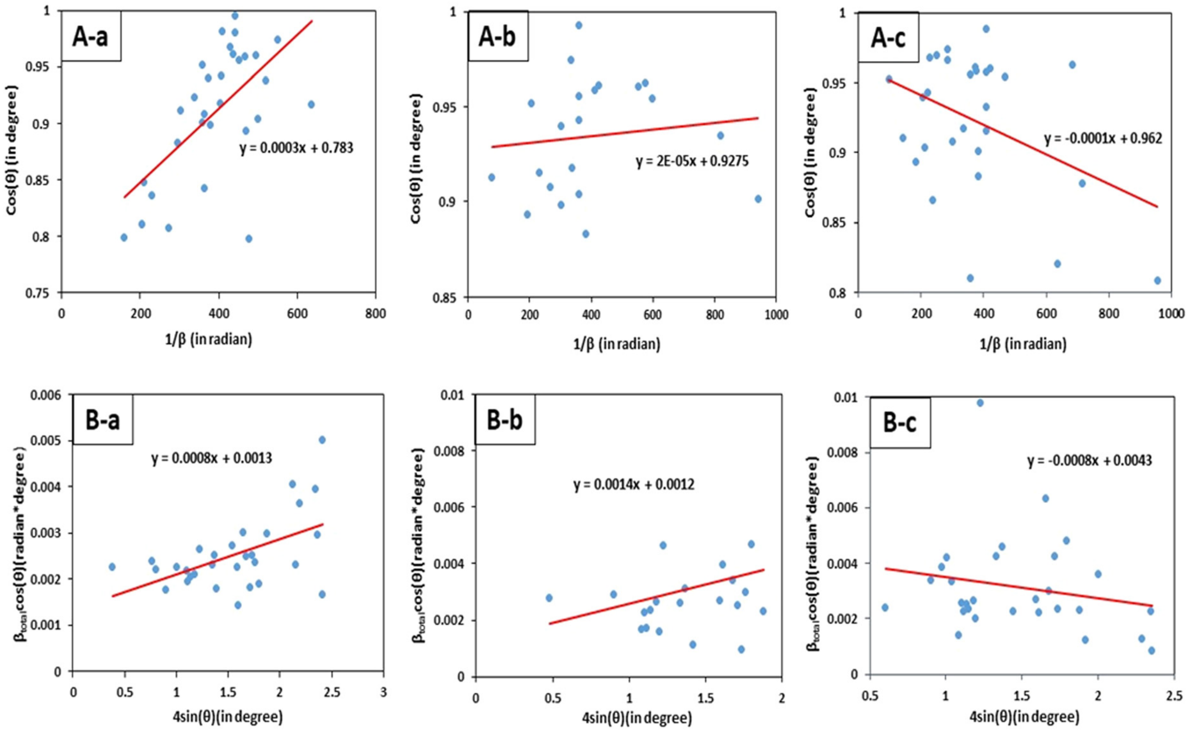

Fig. 2 Graphical representation of (A) the linear straight line method of Scherrer's equation [HAp (A-a), 5 Cu HAp (A-b), and 10 Cu HAp (A-c)] and (B) Williamson–Hall method [HAp (B-a), 5 Cu HAp (B-b), and 10 Cu HAp (B-c)].

Table 2 Crystallite size calculation using various model equations

| Sample name models | Crystallite sizes (nm) HAp | 5-Cu HAp | 10-Cu HAp |
|---|---|---|---|
| Linear straight line method of Scherrer's equation (LSLMSE) | 482.72 | 7240.82 | 1448.16 |
| Williamson–Hall (W–H) method | 66.50 | 52.91 | 42.35 |
| Monshi–Scherrer equation | 65.25 | 61.79 | 56.41 |
| Sahadat–Scherrer model | 65.82 | 76.21 | 72.40 |
| Three peaks average model | 70.13 | 68.47 | 58.86 |

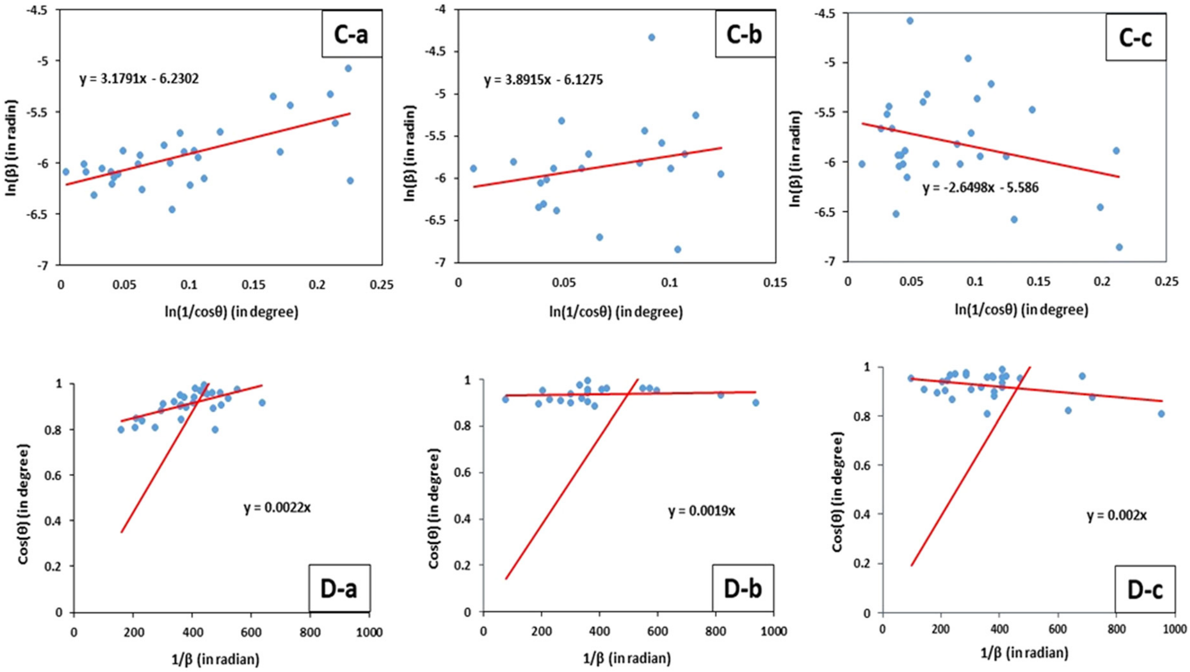

Fig. 3 Graphical scheme of (C) Monshi–Scherrer equation [HAp (C-a), 5 Cu HAp (C-b), and 10 Cu HAp (C-c)] and (D) Sahadat-Scherrer model [HAp (D-a), 5 Cu HAp (D-b), and 10 Cu HAp (D-c)].

### Sahadat–Scherrer model

In this model, the following eqn (20) was used to calculate the crystallite size. The graph shown in Fig. 3(D) was plotted by taking 1/FWHM as the $x$-axis and $\cos\theta$ as the $y$-axis and a straight line was noticed that followed the straight-line equation ($y = mx + c$). With the help of software, Microsoft excel, the intercept was moved to 0 (zero) and the crystallite size was calculated by using the slope $(\frac{K\lambda}{D_C})$ from eqn (20) without intersecting the $y$-axis. The calculated values are indexed in Table 2 and confirmed the validity to measure the crystallite size by using the Sahadat–Scherrer model in the nanoscale range.

$$\cos\,\theta = \frac{K\lambda}{D_{cs}} \times \frac{1}{\text{FWHM}} \tag{20}$$

### Three peaks average model

This model was established with the Scherrer equation and considers the three most intensive diffraction peaks to have discrete average values of $\beta$ (FWHM), $\lambda$ and $\theta$. The most intensive peaks for the HAp samples were recorded as 100% in the (211) plane, 65% in the (300) plane and 47% in the (112) plane according to the standard ICDD database.[48] Taking into account these three planes, the average values of $\beta$ (FWHM), $\theta$ and $\lambda$ were calculated by utilizing the following eqn (21)–(23):

$$\text{B}_{\text{Average}} = \frac{\beta_{211} + \beta_{300} + \beta_{112}}{3} \tag{21}$$

$$\theta_{\text{Average}} = \frac{\theta_{211} + \theta_{300} + \theta_{112}}{3} \tag{22}$$

$$\lambda_{\text{Average}} = \frac{\lambda_{\text{K-alpha1}} + \lambda_{\text{K-alpha2}}}{2} \tag{23}$$

In a copper sourced XRD machine, an X-ray source generates wavelengths at 0.15406 (K-alpha 1), 0.15444 (K-alpha 2) and 0.13922 nm (K-beta). Here, only K-alpha 1 and K-alpha 2 were considered to calculate the average value of $\lambda$, because in modern instrumentation, the effect of K-beta radiation is less when using Ni-filters. The values were then put into Scherrer's equation (eqn (6)) and the results are charted in Table 2 for all the samples. The crystallite sizes obtained by utilizing this model equation are less than 100 nm, which indicates the feasibility of the application of this method to calculate the crystallite size of the HAp samples.

### FT-IR spectral analysis

Fig. 4(a) shows the FT-IR spectra of both the pristine and Cu-doped HAp samples. It is clear that the FT-IR spectra of all three HAp, 5-Cu HAp and 10-Cu HAp samples are almost the same. This is because the main functional groups present in any HAp are $PO_4^{3-}$ and $OH^-$;[34] to analyze the spectra, two regions were considered: (i) 400–1200 $cm^{-1}$, which is distinctive for the phosphate group; and (ii) 3000–3800 $cm^{-1}$, which is representative of the hydroxyl group.[28,49]

Details of the registered band positions and their analogous assignments are presented in Table 3. Clearly, in Table 3, the customary band positions for the $PO_4^{3-}$ group were noticeable, as mentioned elsewhere.[36,37] On the other hand, the bands responsible for apatitic hydroxyl groups were also in good agreement with previous results.[50] However, nearly the same intensity of the hydroxyl group's absorption bands was observed in all three cases (Fig. 4(b)), showing the zoom in format of the IR region (3000–4000 $cm^{-1}$), which demonstrates that copper ions did not substitute the hydrogens of the $OH^-$ group in the hexagonal channels.[28]

This observation also supplements the XRD analysis, which found that the Cu substitution occurs at $Ca_1$ sites but not $OH^-$ groups.

Since crystallinity index (CI) is considered to be a quantitative indicator of crystallinity and, like XRD, FT-IR data also permit the crystallinity index to be measured,[51] we further attempted to calculate the crystallinity index (CI) *via* eqn (24)–(28).[35,52]

$$\mathrm{CI}_{\mathrm{height}} = \frac{A_{565} + A_{605}}{A_{595}} \tag{24}$$

$$\mathrm{CI}_{\mathrm{area(1060)}} = \frac{A_{1060}}{A_{900-1200}} \tag{25}$$

$$\mathrm{CI}_{\text{area-603}} = \frac{A_1}{A_2} \tag{26}$$

$$\mathrm{CI}_{\text{FWHM-603}} = \mathrm{FWHM}_{603} \tag{27}$$

$$\mathrm{CI}_{\text{FWHM-1028}} = \mathrm{FWHM}_{1028} \tag{28}$$

Here, in eqn (24), $\mathrm{CI}_{\mathrm{height}}$ denotes the crystallinity index as calculated using FT-IR data. $A_{565}$, $A_{603}$ and $A_{595}$ represent the corresponding height of the peaks at 565, 505 and 595 $cm^{-1}$. In eqn (25), $A_{1060}$ and $A_{900-1200}$ are the areas of the corresponding peak and section while the total area ($A_1$) and the splitting area ($A_2$) measured for the phosphate groups around 603 $cm^{-1}$ were used to calculate $\mathrm{CI}_{\text{area-603}}$. Eqn (27) and (28) are based on the measurement of FWHM, and $\mathrm{FWHM}_{603}$ and $\mathrm{FWHM}_{1028}$ define the respective values at 603 and 1028 $cm^{-1}$. All these data calculated using the FT-IR spectra are included in Table 4, which shows that due to copper incorporation, the crystallinity decreases as the value of FWHM increases (Fig. 4(c)).

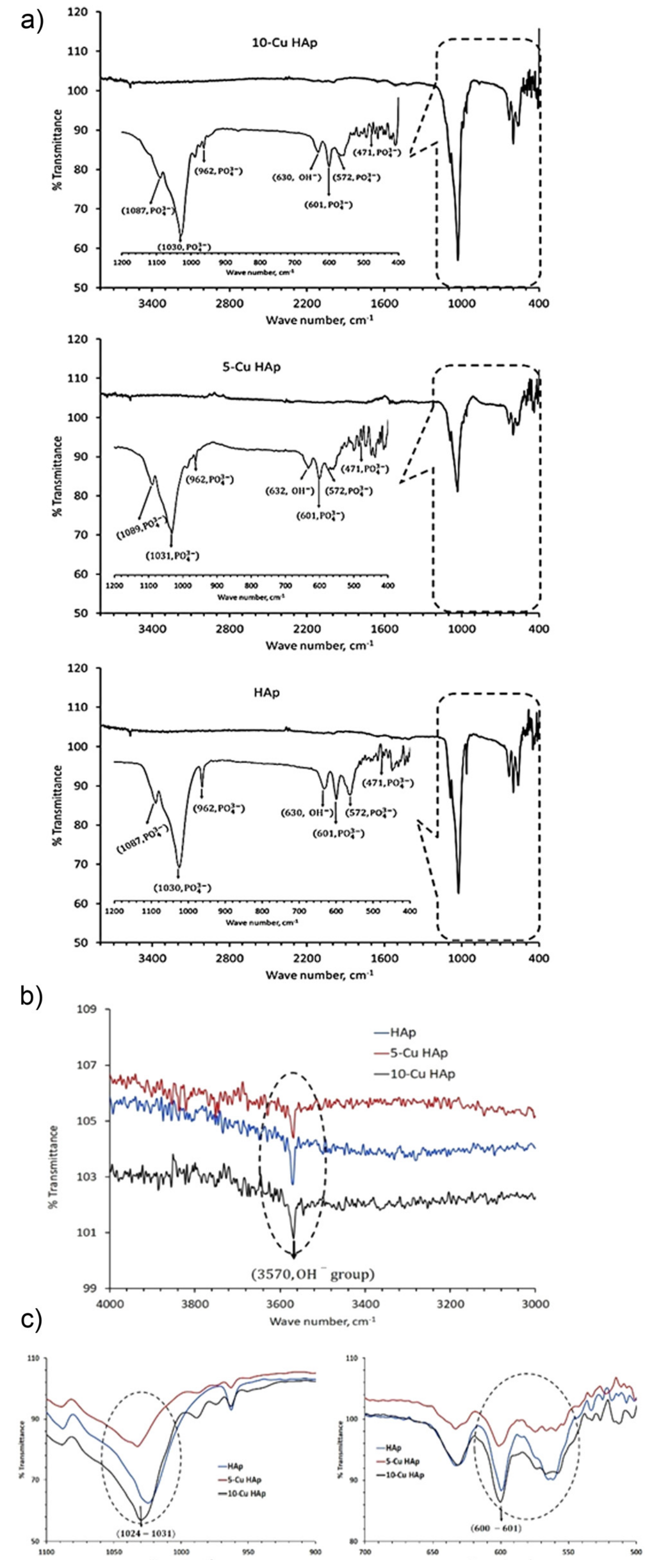

Fig. 4 (a) FT-IR spectra of pure and copper doped HAp. (b) Zoom in form of the IR region of 3000–4000 $cm^{-1}$. (c) Zoom in form of the IR regions of 900–1100 $cm^{-1}$ and 500–700 $cm^{-1}$.

Table 3 FT-IR band positions of HAp, 5-Cu HAp and 10-Cu HAp and the respective assignments

| Characteristic group | Band position, $\mathrm{cm}^{-1}$ | Characteristic assignment |
|---|---|---|
| $\mathrm{PO_4}^{3-}$ | 472 | $\nu_2$, symmetric bending |
| | 572 | $\nu_4$, asymmetric bending |
| | 601 | $\nu_4$, asymmetric bending |
| | 962 | $\nu_1$, symmetric stretching |
| | 1030 | $\nu_3$, asymmetric stretching |
| | 1087 | $\nu_3$, asymmetric stretching |
| $\mathrm{OH}^-$ group | 630 | $\mathrm{OH}^-$, vibrational |
| | 3570 | Apatitic $\mathrm{OH}^-$, stretching |

Table 4 Crystallinity index for HAp, 5-Cu Hap, and 10-Cu Hap based on FT-IR data

| Method | HAp | 5Cu-HAp | 10Cu-HAp |
|---|---|---|---|
| $\mathrm{CI}_{\mathrm{height}}$ | 9.94 | 3.39 | 5.07 |
| $\mathrm{CI}_{\mathrm{area\text{-}1060}}$ | 0.72 | 0.55 | 0.49 |
| $\mathrm{CI}_{\mathrm{area\text{-}603}}$ | 1.80 | 2.64 | 2.97 |
| $\mathrm{CI}_{\mathrm{FWHM\text{-}603}}$ | 66.912 | 67.57 | 79.08 |
| $\mathrm{CI}_{\mathrm{FWHM\text{-}1028}}$ | 66.40 | 95.06 | 97.79 |

### FESEM and EDS analyses

FESEM images showed that the particles of Cu-doped Hap samples were nanometer sized but mostly agglomerated. In contrast, EDS analysis enabled the chemical compositions of the synthesized Cu-doped samples to be determined. However, for both samples, the presence of Cu along with Ca, P and O was visualised as expected. The amount of Cu in 5-Cu Hap and 10-Cu Hap was 2.01 and 2.6 At%, respectively (Fig. 5).

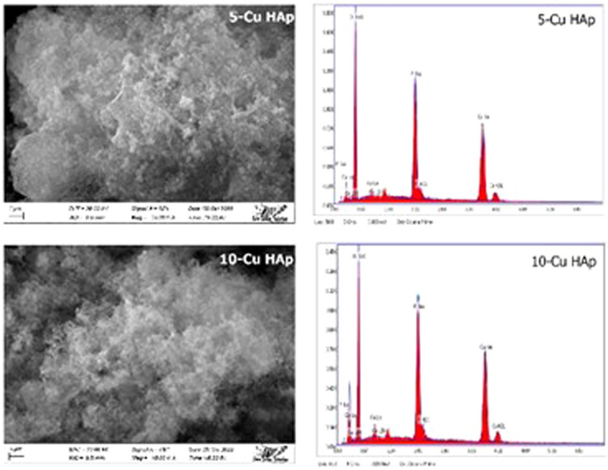

Fig. 5 FESEM and EDS results of Cu-doped hydroxyapatite samples.

### Biomedical compatibility

**Haemolysis test.** For the sustainable application of HAp as a biomaterial, haemocompatibility is an important parameter to be checked before implementation because haemolysis releases iron (Fe) due to the breakdown of red blood cells (RBCs), which causes serious haemolytic anemia in the human body. To check the haemocompatible nature of the pure and Cu doped HAp samples, the resultant haemolysis percentage was placed into three different categories: (i) highly haemocompatible (less than 5%), (ii) haemocompatible (less than 10%) and (iii) non-haemocompatible (greater than 20%), according to the standard ASTM method.[53] Fig. 6 shows an outstanding result of haemocompatibility of each sample with a very high dose (500 μg $\mathrm{mL}^{-1}$), where the maximum result was observed in the case of 10 Cu HAp (6.85%) and can be categorized as haemocompatible. A very good result of 1.47% was recorded for pure Hap, 4.93% was obtained for 5 Cu HAp and both showed a highly haemocompatible nature for the lysis of RBCs. Despite its relatively higher haemolysis percentage, the value for 10 Cu HAp remained in an acceptable range and thus all the synthesized HAp samples can be used as a safe biomaterial.

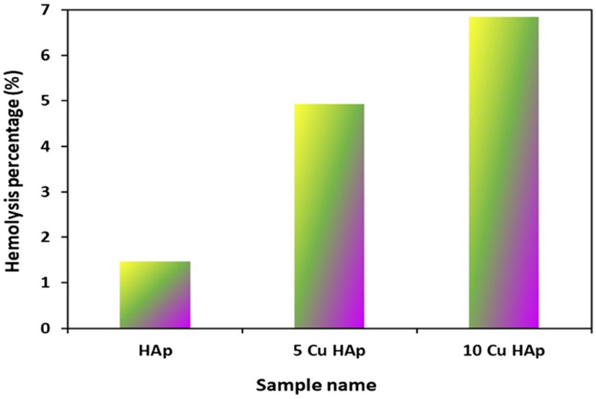

Fig. 6 Haemolytic percentage at a very high dose of 500 μg $\mathrm{mL}^{-1}$ of the pure HAp and Cu doped HAp samples.

### Cytotoxicity assessment

A cytotoxicity test was carried out to determine the biocompatible character of the HAp and Cu doped HAp as they can cause cell death when exposed at a toxic level to living cells. The test was executed at a slightly higher dose of 100 μg $\mathrm{mL}^{-1}$ and as a control the reference standard dimethyl sulfoxide (DMSO) was used. The other conditions are described in the methodology section. Pictorial aspects of the control and prepared samples captured after 72 hours of incubation are exhibited in Fig. 7. The visibility of the pictures was adjusted with the standard data and they provide a good affirmation for using pure and Cu doped HAp as an inherent biomaterial in biomedical fields. A graphical scheme is presented in Fig. 8 that shows the cell viability percentage of the synthesized HAp samples. A superb percentage of cell viability was obtained wherein the pure HAp sample showed 96.4% cell viability, which was almost the same as the control value (97.2%). The doped materials were found to show a relatively slight decrease (90.8% and 92.6% for 5 and 10 Cu HAp, respectively) in the percentage but stayed in the tolerable region. According to the ISO 10993-5 standard, all the obtained values were within the non-cytotoxic range and represent a good biocompatible character with the human body cell. So, pure HAp along with 5% and 10% Cu doped HAp can be considered as superior implant materials with a satisfactory cytotoxicity level.

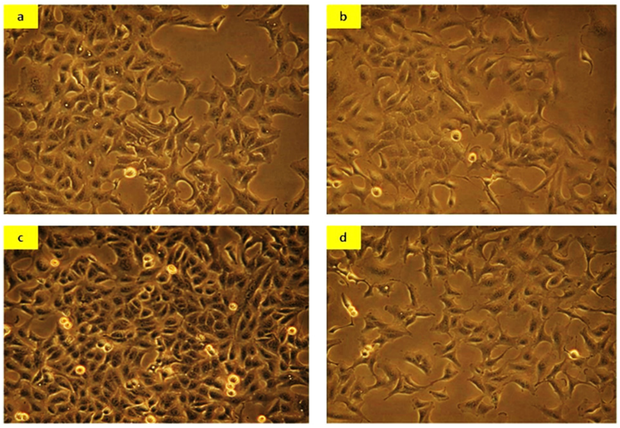

Fig. 7 Influence of cytotoxicity on (a) dimethyl sulfoxide (control), (b) pure HAp, (c) 5-Cu HAp, and (d) 10-Cu Hap.

### Antimicrobial activity

Pictorial views of the antimicrobial activity of the pure and Cu doped HAp samples are shown in Fig. 9, which was evaluated by using *S. aureus* (Gram positive bacteria) and *E. coli* (a Gram negative bacteria). *S. aureus* and *E. coli* exhibited no significant distinct interaction with the Cu doped HAp samples or the pure HAp samples. The Gram positive bacteria (*S. aureus*) could not hinder the formation of colonies in the case of pure and 10 Cu HAp. The maximum number of colonies formed with the pure HAp due to the release of hydroxyl ($OH^-$) ions, which act as a strong free radical in aqueous solution with higher reactivity, and relatively lesser antimicrobial activity than the 10 Cu HAp sample. An excellent result was noticed with no colony formation for 5% Cu doped HAp. On the other hand, the Gram negative bacteria (*E. coli*) formed colonies with both Cu doped HAp samples but a very negligible number of colonies were formed in the case of 5 Cu HAp and relatively fewer colonies were observed with 10 Cu HAp compared to *S. aureus* bacteria. The variation in colony formation between these two Cu doped HAp samples may be due to their crystallite size as the number of ions produced and microbial properties rely on size.[54] Thus, the antimicrobial property of the prepared samples can be ordered from strong to weak in the following way: 5 Cu Hap > 10 Cu HAp > pure HAp. There was no noticeable difference, so we were unable to compute the number of colonies formed with the two chosen bacteria.

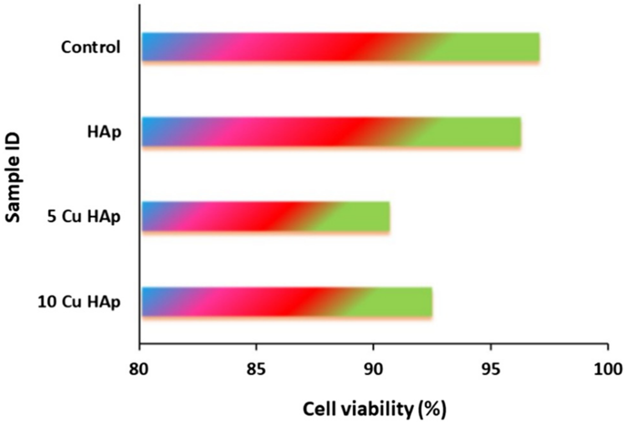

Fig. 8 Percentage cell viability of the synthesized HAp samples and control (DMSO).

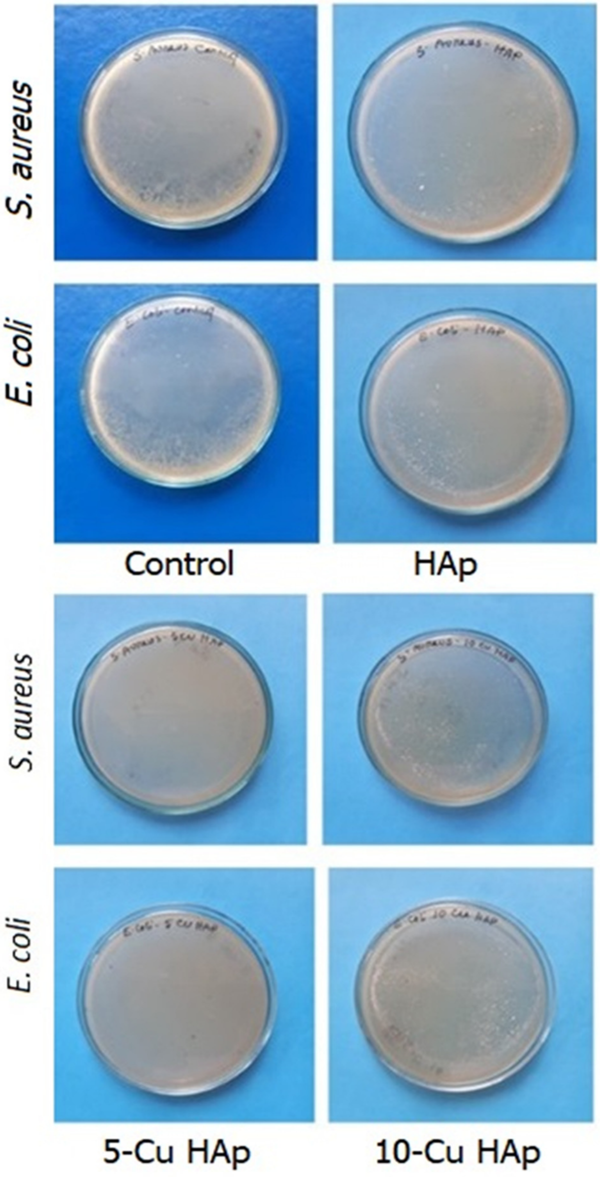

Fig. 9 Photographic presentation of antibacterial activity of the pure and Cu doped HAp samples.

The properties of crystalline materials mainly depend on the structure of the crystal. When doping materials are used, the crystallographic structure of the materials is greatly changed. From the previously reported results, it is clear that the doping of copper metal in the hydroxyapatite structure changes the crystallographic parameters. The variation in crystallographic parameters ultimately affects the properties of biomaterials; in this case, cytotoxicity, haemolysis and antimicrobial characters. For example, the crystallite size of the hydroxyapatite biomaterial is larger than that of the 5% copper doped hydroxyapatite. This small size of the crystal ultimately increases the surface area along with the surface energy, which affect the cytotoxicity phenomenon by curtailing the cell viability. A similar affect was also noticed for the Gram-positive and Gram-negative bacteria. When 5% copper was doped, all bacterial colonies were destroyed. There is another reason for the destruction of more microbes along with the crystallite size and that is the antimicrobial properties of nano sized copper. Among the reported three biomaterials, the 5% copper doped sample presented the best results in terms of cytotoxicity, haemolysis and antimicrobial activity. The antimicrobial activity of the pure hydroxyapatite is very low, thus copper was doped to increase this property. The addition of copper into the HAp crystal increased the antimicrobial property compared to the pure form. But, 10% Cu-HAp revealed a relatively lower antimicrobial activity than 5% copper HAp. Thus, it cannot always be true that the addition of a metal into pure biomaterials can impart excellent antimicrobial properties. There are a number of crystallographic parameters that contributed to the antimicrobial activity in addition to the cytotoxicity and haemolysis behavior. Considering all the crystallographic parameters, such as lattice parameters, crystallinity index, dislocation density, degree of crystallinity, microstrain, HAp percentage, crystallite size (including the Monshi–Scherrer, Sahadat–Scherrer, Williamson–Hall, straight-line, and three peaks models), specific surface area, cell volume, growth preference and relative intensity obtained from XRD and FT-IR analysis, the 5% copper doped HAp was optimized for application as a biomaterial. These findings also supported the relationship of crystallographic parameters with the properties of biomaterials such as cytotoxicity, haemolysis and antimicrobial activity.

## Conclusion

The crystallographic parameters provide good evidence that copper doped hydroxyapatite can be used as a biomaterial. For the safe and sound applicability of Cu-doped HAp, we examined the haemolysis and cytotoxicity properties, which revealed positive results. Moreover, the performance of Cu-doped HAp while examining the antimicrobial activity revealed considerably acceptable results for biomedical fields. The data presented a remarkable result in the case of 5% Cu doped HAp with a very high dose of sample materials when biocompatibility was assessed. There remained a relationship among the crystallographic parameters and Cu-metal doping in the biomaterial for efficient applications of biomaterials considering cytotoxicity, haemolysis and antimicrobial activity. It is suggested from this research work that 5% copper doped hydroxyapatite (HAp) has potential as a biomaterial for application in biomedical fields.

## Statements and declarations

The authors declare that this manuscript has neither been submitted elsewhere nor is under consideration in any other journal.

## Author contributions

Supanna Malek Tuntun synthesized and characterized the pure and copper doped hydroxyapatite, wrote the original manuscript, analysed the data and prepared a draft of the manuscript. Md. Sahadat Hossain conceived and designed the experiment, performed the experiment and took part in preparing the draft of the manuscript along with Supanna Malek Tuntun. Md. Najem Uddin executed the cytotoxicity, haemolysis and antimicrobial assessment. Newaz Mohammed Bahadur and Samina Ahmed supervised the findings of this work. Md. Aftab Ali Shaikh contributed to the FT-IR, FESEM and EDS analyses as well as writing the manuscript. Samina Ahmed supervised the overall work and assisted in writing the manuscript.

## Conflicts of interest

The authors have no relevant financial or non-financial interests to disclose.

## Acknowledgements

The authors are grateful to the Bangladesh Council of Scientific and Industrial Research (BCSIR) authority for financial support through R&D project (ref. no. 39.02.0000.011.14.134.2021/900; Date: 30.12.2021). The authors are also grateful to Ministry of Science and Technology for financial support through NST fellowship (ref. no. 39.00.0000.012.002.06.20-72; Date: 02.06.2022). Md. Najem Uddin wishes to thank Pharmaceutical Research Division, BCSIR laboratories Dhaka, for executing the cytotoxicity, haemolysis and antimicrobial assessment. Supanna Malek Tuntun wishes to thank Department of Applied Chemistry and Chemical Engineering, Noakhali Science and Technology University, Noakhali, Bangladesh for approving M.S. Thesis program. We thank Muhammad Shahriar Bashar, Principal Scientific Officer, Institute of Fuel Research and Development, BCSIR for all his support.

## References

1 A. Camaioni, I. Cacciotti, L. Campagnolo and A. Bianco, Silicon-substituted hydroxyapatite for biomedical applications, *Hydroxyapatite (Hap) for Biomedical Applications*, Elsevier, 2015, pp. 343–373, DOI: **10.1016/B978-1-78242-033-0.00015-8**.
2 A. A. Majhool, I. Zainol, S. S. S. A. Azziz, C. N. A. Jaafar and M. M. Jahil, Mechanical properties improvement of epoxy composites by natural hydroxyapatite from fish scales as a fillers, *Int. J. Res. Pharm. Sci.*, 2019, **10**(2), 1424–1429.
3 M. Miranda, *et al.*, Silver-hydroxyapatite nanocomposites as bactericidal and fungicidal materials, *Int. J. Mater. Res.*, 2010, **101**(1), 122–127.
4 M. Sadat-Shojai, M. Atai, A. Nodehi and L. N. Khanlar, Hydroxyapatite nanorods as novel fillers for improving the properties of dental adhesives: Synthesis and application, *Dent. Mater.*, 2010, **26**(5), 471–482.

5 J. Wang and L. L. Shaw, Nanocrystalline hydroxyapatite with simultaneous enhancements in hardness and toughness, *Biomaterials*, 2009, **30**(34), 6565–6572.

6 Y. Zhu, L. Xu, C. Liu, C. Zhang and N. Wu, Nucleation and growth of hydroxyapatite nanocrystals by hydrothermal method, *AIP Adv.*, 2018, **8**(8), 085221.

7 P. A. F. Sossa, B. S. Giraldo, B. C. G. Garcia, E. R. Parra and P. J. A. Arango, Comparative study between natural and synthetic Hydroxyapatite: structural, morphological and bioactivity properties, *Matéria (Rio de Janeiro)*, 2018, **23**(4), 12217, DOI: **10.1590/S1517-707620180004.0551**.

8 N. Rameshbabu, K. P. Rao and T. S. Kumar, Acclerated microwave processing of nanocrystalline hydroxyapatite, *J. Mater. Sci.*, 2005, **40**(23), 6319–6323.

9 J. Venugopal, M. P. Prabhakaran, Y. Zhang, S. Low, A. T. Choon and S. Ramakrishna, Biomimetic hydroxyapatite-containing composite nanofibrous substrates for bone tissue engineering, *Philos. Trans. R. Soc., A*, 2010, **368**(1917), 2065–2081.

10 J. Venugopal, P. Vadgama, T. S. Kumar and S. Ramakrishna, Biocomposite nanofibres and osteoblasts for bone tissue engineering, *Nanotechnology*, 2007, **18**(5), 055101.

11 R. M. Ottenbrite, S. J. Huang and K. Park, *Hydrogels and biodegradable polymers for bioapplications*, ACS Publications, 1996, vol. 627.

12 B. Dhandayuthapani and D. Sakthi kumar, Biomaterials for Biomedical Applications, *Biomedical Applications of Polymeric Materials and Composites*, John Wiley & Sons, Ltd, 2016, pp. 1–20, DOI: **10.1002/9783527690916.ch1**.

13 F. M. Veronese, F. Marsilio, S. Lora, P. Caliceti, P. Passi and P. Orsolini, Polyphosphazene membranes and microspheres in periodontal diseases and implant surgery, *Biomaterials*, 1999, **20**(1), 91–98.

14 P. Caliceti, *et al.*, Bioabsorbable polyphosphazene matrices as systems for calcitonin controlled release, *Farmaco*, 1997, **52**(11), 697–702.

15 J. Wang, P. C. Zhang, H. Q. Mao and K. W. Leong, Enhanced gene expression in mouse muscle by sustained release of plasmid DNA using PPE-EA as a carrier, *Gene Ther.*, 2002, **9**(18), 1254–1261.

16 Y. Zhu, C. Gao, T. He and J. Shen, Endothelium regeneration on luminal surface of polyurethane vascular scaffold modified with diamine and covalently grafted with gelatin, *Biomaterials*, 2004, **25**(3), 423–430.

17 P. A. Gunatillake, R. Adhikari and N. Gadegaard, Biodegradable synthetic polymers for tissue engineering, *Eur. Cells Mater.*, 2003, **5**(1), 1–16.

18 D. Cohn and A. H. Salomon, Designing biodegradable multiblock PCL/PLA thermoplastic elastomers, *Biomaterials*, 2005, **26**(15), 2297–2305.

19 L. L. Hench, R. J. Splinter, W. C. Allen and T. K. Greenlee, Bonding mechanisms at the interface of ceramic prosthetic materials, *J. Biomed. Mater. Res.*, 1971, **5**(6), 117–141.

20 V. Uskoković, Ion-doped hydroxyapatite: An impasse or the road to follow?, *Ceram. Int.*, 2020, **46**(8), 11443–11465, DOI: **10.1016/j.ceramint.2020.02.001**.

21 S. Kim and M. Kim, A new species of Fimbristylis (Cyperaceae): F. jindoensis J. Kim & M. Kim, *Korean J. Pl. Taxon.*, 2012, 318–322.

22 C. Robinson, R. C. Shore, S. J. Brookes, S. Strafford, S. R. Wood and J. Kirkham, The chemistry of enamel caries, *Crit. Rev. Oral Biol. Med.*, 2000, **11**(4), 481–495.

23 R. H. Petrov, *et al.*, Three dimensional microstructure–microtexture characterization of pipeline steel, *Mater. Sci. Forum*, 2007, **550**, 625–630.

24 M. Kawashita, S. Tsuneyama, F. Miyaji, T. Kokubo, H. Kozuka and K. Yamamoto, Antibacterial silver-containing silica glass prepared by sol–gel method, *Biomaterials*, 2000, **21**(4), 393–398.

25 M. H. Santos, P. Valerio, A. M. Goes, M. F. Leite, L. G. D. Heneine and H. S. Mansur, Biocompatibility evaluation of hydroxyapatite/collagen nanocomposites doped with $Zn^{2+}$, *Biomed. Mater.*, 2007, **2**(2), 135.

26 A. Ito, K. Ojima, H. Naito, N. Ichinose and T. Tateishi, Preparation, solubility, and cytocompatibility of zinc-releasing calcium phosphate ceramics, *J. Biomed. Mater. Res.*, 2000, **50**(2), 178–183.

27 S. Dasgupta, A. Bandyopadhyay and S. Bose, Zn and Mg Doped Hydroxyapatite Nanoparticles for Controlled Release of Protein, *Langmuir*, 2010, **26**(7), 4958–4964, DOI: **10.1021/la903617e**.

28 T. Bazin, *et al.*, Sintering and biocompatibility of copper-doped hydroxyapatite bioceramics, *Ceram. Int.*, 2021, **47**(10), 13644–13654.

29 S. Shanmugam and B. Gopal, Copper substituted hydroxyapatite and fluorapatite: Synthesis, characterization and antimicrobial properties, *Ceram. Int.*, 2014, **40**(10), 15655–15662.

30 R. B. Unabia, S. Bonebeau, R. T. Candidato Jr, J. Jouin, O. Noguera and L. Pawłowski, Investigation on the structural and microstructural properties of copper-doped hydroxyapatite coatings deposited using solution precursor plasma spraying, *J. Eur. Ceram. Soc.*, 2019, **39**(14), 4255–4263.

31 A. Ressler, A. Žužić, I. Ivanišević, N. Kamboj and H. Ivanković, Ionic substituted hydroxyapatite for bone regeneration applications: A review, *Open Ceram.*, 2021, **6**, 100122.

32 S. Gomes, *et al.*, Cu-doping of calcium phosphate bioceramics: From mechanism to the control of cytotoxicity, *Acta Biomater.*, 2018, **65**, 462–474.

33 N. V. Eremina, S. V. Makarova, D. D. Isaev and N. V. Bulina, Soft mechanochemical synthesis and thermal stability of hydroxyapatites with different types of substitution, *Chim. Techno Acta*, 2022, **9**(3), 20229305.

34 M. Hossain, M. Mahmud, M. B. Mobarak and S. Ahmed, Crystallographic analysis of biphasic hydroxyapatite synthesized by different methods: an appraisal between new and existing models, *Chem. Pap.*, 2022, **76**(3), 1593–1605.

35 M. S. Hossain, M. A. A. Shaikh, M. S. Rahaman and S. Ahmed, Modification of the crystallographic parameters in a biomaterial employing a series of gamma radiation

doses, *Mol. Syst. Des. Eng.*, 2022, **7**, 1239–1248, DOI: 10.1039/D2ME00061J.

36 A. Basu, *et al.*, Polyphenol capping on a gold nanosurface modulates human serum albumin fibrillation, *Mater. Adv.*, 2020, **1**(5), 1142–1150.

37 S. Sultana, *et al.*, UV-assisted synthesis of hydroxyapatite from eggshells at ambient temperature: cytotoxicity, drug delivery and bioactivity, *RSC Adv.*, 2021, **11**(6), 3686–3694.

38 S. Stagnoli, *et al.*, Unique catanionic vesicles as a potential 'Nano-Taxi' for drug delivery systems. *In vitro* and *in vivo* biocompatibility evaluation, *RSC Adv.*, 2017, **7**(9), 5372–5380.

39 V. P. Padmanabhan, S. N. TSN, S. Sagadevan, M. E. Hoque and R. Kulandaivelu, Advanced lithium substituted hydroxyapatite nanoparticles for antimicrobial and hemolytic studies, *New J. Chem.*, 2019, **43**(47), 18484–18494.

40 Z. Yang, *et al.*, Promotional effect of lanthana on the high-temperature thermal stability of Pt/$TiO_2$ sulfur-resistant diesel oxidation catalysts, *RSC Adv.*, 2017, **7**(31), 19318–19329.

41 K. V. Kumar, *et al.*, Spectral characterization of hydroxyapatite extracted from Black Sumatra and Fighting cock bone samples: A comparative analysis, *Saudi J. Biol. Sci.*, 2021, **28**(1), 840–846.

42 M. Sharma, R. Nagar, V. Kumar Meena and S. Singh, Electro-deposition of bactericidal and corrosion-resistant hydroxyapatite nanoslabs, *RSC Adv.*, 2019, **9**(20), 11170–11178, DOI: 10.1039/C9RA00811J.

43 S. P. Muhoza, T. H. Taylor, X. Song and M. D. Gross, The Impact of Sintering Atmosphere and Temperature on the Phase Evolution of High Surface Area LSCF Prepared by In Situ Carbon Templating, *J. Electrochem. Soc.*, 2021, **168**(3), 034519.

44 M. Hossain, *et al.*, New analytical models for precise calculation of crystallite size: application to synthetic hydroxyapatite and natural eggshell crystalline materials, *Chem. Pap.*, 2022, 1–7.

45 M. Rabiei, A. Palevicius, A. Monshi, S. Nasiri, A. Vilkauskas and G. Janusas, Comparing Methods for Calculating Nano Crystal Size of Natural Hydroxyapatite Using X-Ray Diffraction, *Nanomaterials*, 2020, **10**(9), 1627, DOI: 10.3390/nano10091627.

46 D. Nath, F. Singh and R. Das, X-ray diffraction analysis by Williamson-Hall, Halder-Wagner and size-strain plot methods of CdSe nanoparticles- a comparative study, *Mater. Chem. Phys.*, 2020, **239**, 122021, DOI: 10.1016/j.matchemphys.2019.122021.

47 A. Monshi, M. R. Foroughi and M. R. Monshi, Modified Scherrer Equation to Estimate More Accurately Nano-Crystallite Size Using XRD, *World J. Nano Sci. Eng.*, 2012, **02**(03), 154–160, DOI: 10.4236/wjnse.2012.23020.

48 M. Markovic, B. O. Fowler and M. S. Tung, Preparation and comprehensive characterization of a calcium hydroxyapatite reference material, *J. Res. Natl. Inst. Stand. Technol.*, 2004, **109**(6), 553.

49 N. V. Bulina, N. V. Eremina, O. B. Vinokurova, A. V. Ishchenko and M. V. Chaikina, Diffusion of Copper Ions in the Lattice of Substituted Hydroxyapatite during Heat Treatment, *Materials*, 2022, **15**(16), 5759.

50 M. Petra, J. Anastassopoulou, T. Theologis and T. Theophanides, Synchrotron micro-FT-IR spectroscopic evaluation of normal paediatric human bone, *J. Mol. Struct.*, 2005, **733**(1–3), 101–110.

51 J. Reyes-Gasga, E. L. Martínez-Piñeiro, G. Rodríguez-Álvarez, G. E. Tiznado-Orozco, R. García-García and E. F. Brès, XRD and FTIR crystallinity indices in sound human tooth enamel and synthetic hydroxyapatite, *Mater. Sci. Eng., C*, 2013, **33**(8), 4568–4574.

52 Y. Sa, *et al.*, Are different crystallinity-index-calculating methods of hydroxyapatite efficient and consistent?, *New J. Chem.*, 2017, **41**(13), 5723–5731.

53 V. S. Chandra, *et al.*, Synthesis of magnetic hydroxyapatite by hydrothermal–microwave technique: Dielectric, protein adsorption, blood compatibility and drug release studies, *Ceram. Int.*, 2015, **41**(10), 13153–13163.

54 P. N. Silva-Holguín and S. Y. Reyes-López, Synthesis of Hydroxyapatite–Ag Composite as Antimicrobial Agent, *Dose-Response*, 2020, **18**(3), 1559325820951342, DOI: 10.1177/1559325820951342.